# TIME-LINEARIZED ANALYSIS OF MOTION-INDUCED AND GUST-INDUCED AIRLOADS WITH THE DLR TAU CODE

C. Kaiser, R. Thormann, D. Dimitrov, J. Nitzsche
German Aerospace Center (DLR)
37073 Göttingen
Germany

**Abstract**

This paper provides an overview about the time-linearized analysis of motion-induced and gust-induced airloads with the DLR flow solver TAU. Time-linearized CFD methods to compute an aircraft's aerodynamic response to sinusoidal oscillations promise a reduced computational effort while retaining the fidelity of the RANS flow characteristics. Two approaches are presented: a system identification method which excites the nonlinear steady background flow state with a broad-band pulse signal of small amplitude resulting in the aerodynamic frequency response function, and the DLR TAU linear frequency domain (LFD) solver which solves the linearized and Fourier transformed unsteady RANS equations for the first harmonic of the aerodynamic response. Both methods are validated with forced-motion pitching oscillations of the 2-d NACA 64A010 airfoil in comparison to the response of the fully nonlinear solver. Furthermore, the pulse method and LFD method are extended for sinusoidal gust encounters

## NOMENCLATURE

| | | |
|---|---|---|
| $\alpha$ | = | incidence angle |
| $c$ | = | chord length |
| $C_l$ | = | lift coefficient |
| $Ma_\infty$ | = | freestream Mach number |
| $\lambda$ | = | wave length, pulse length |
| $\phi$ | = | phase angle |
| $Re_\infty$ | = | freestream Reynolds number |
| $T$ | = | oscillation period, simulation time |
| $U_\infty$ | = | freestream velocity |
| $\boldsymbol{v}_g$ | = | grid-node velocities |
| $\omega^{(*)}$ | = | (reduced) angular frequency |
| $\boldsymbol{x}$ | = | grid-node coordinates |

Superscripts:

| | | |
|---|---|---|
| $\dot{}$ | = | temporal derivative $\partial/\partial t$ |
| $\bar{}$ | = | time-invariant mean state |
| $\hat{}$ | = | perturbation amplitude, Fourier coefficient |

Abbreviations:

| | | |
|---|---|---|
| ALE | = | arbitrary Lagrangian-Euler formulation |
| DVA | = | disturbance velocity approach |
| FRF | = | frequency response function |
| LFD | = | linear frequency domain solver |
| RHS | = | right-hand-side vector |

## 1. INTRODUCTION

The numerical evaluation of unsteady airloads employing high-fidelity Reynolds-averaged Navier-Stokes (RANS) methods already implies high computational effort. Moreover, the analysis of flutter stability of an aircraft or the analysis of the maximum loads due to gust encounters requires a large number of simulations in a huge parameter space comprising the steady aeroelastic trim state at various mass configurations, the Mach number and altitude for which the aerodynamic response to oscillatory deflections of the elastic mode shapes need to be considered at multiple frequencies. Time-linearized CFD methods aiming at the computation of the aircraft's aerodynamic response to small-amplitude oscillatory perturbations promise a reduction of computational effort while retaining the fidelity of the RANS flow solution [1]. In contrast, today's state-of-the-art highly efficient unsteady aerodynamic analysis methods like the doublet-lattice method (DLM) [2] are based on compressible acceleration potential theory that do not account for effects of wing thickness, recompression shocks and boundary layer laminar-turbulent transition or flow separation.

Flutter stability analysis is commonly conducted in the frequency domain on the basis of linear aerodynamic transfer functions that relate a rigid-body or elastic deflection input to the output response of a generalized aerodynamic force. The linear frequency domain approach is suited here because small disturbances are sufficient for predicting the stability of the fluid-structure-coupled aircraft system. Forced-motion simulations of harmonic excitation are employed in order to obtain the transfer functions at the excitation frequencies. In contrast, gust load analyses are commonly conducted in the time domain to safely determine the instant peak loads in the time-accurate response of the combined aerodynamic and inertial loads. Furthermore, while the flutter problem is inherently limited to the consideration of *small* oscillatory perturbations of the steady state, the gust response of an aircraft typically yields *large* perturbations and linearity can no longer be assumed. However, experience shows that a linearized approach leads to conservative results in most cases and under the assumption of superposition sinusoidal gust simulations at small amplitude can be used to construct the actual gust response by inverse Fourier transformation.

Two approaches to perform the time-linearized analysis are presented. First a method of system identification is applied. Therefore, a steady-state RANS solution is

excited with a broadband, short-time signal of very small amplitude. Due to the small-amplitude perturbation on the steady mean state, the dynamic response can be considered as linear and, hence, a frequency response function (FRF) can be derived. The second approach is the linear frequency domain solver (LFD) [3] of the DLR TAU code which solves the time-linearized system of discretized RANS equations. Therefore, the unsteady RANS equations are linearized around the steady state, transformed into the frequency domain and directly solved for the first harmonic of the flow's response.

At first, the governing equations with the necessary extension for forced-motion and gust simulations are presented along with the two time-linearized approaches. Both methods are validated by comparing the obtained FRF for NACA 64A010 pitch oscillations with the Fourier-transformed response of the dynamically nonlinear time-accurate simulation. The LFD solver is additionally extended and validated for sinusoidal gust encounters.

## 2. NUMERICAL METHODS

### 2.1. Governing Equations

The governing equations of DLR's flow solver TAU [4] are the unsteady Reynolds-averaged Navier-Stokes (URANS) equations with an eddy-viscosity closure provided by a turbulence model and with an arbitrary Lagrangian-Euler (ALE) extension introducing grid-node velocities [5]. They are expressed for an open physical domain $\Omega$ in an integral conservation form:

$$(1)\quad \frac{d}{dt}\int_{\Omega(t)} \boldsymbol{W}\, d|\Omega| + \boldsymbol{R}\left(\boldsymbol{W}, \boldsymbol{x}, \boldsymbol{v}_g\right) = 0$$

The state vector $\boldsymbol{W}$ consists of the conservative variables of the flow assuming a calorically perfect gas and the variables of the turbulence closure. The residual $\boldsymbol{R}$ depends on the time-dependent coordinates $\boldsymbol{x}(t)$ and the grid-node velocities $\boldsymbol{v}_g(t)$:

$$(2)\quad \boldsymbol{R}\left(\boldsymbol{W}, \boldsymbol{x}, \boldsymbol{v}_g\right) = \int_{\partial\Omega(t)} (\boldsymbol{f} - \boldsymbol{W}\boldsymbol{v}_g)\cdot \boldsymbol{n}\, d|\partial\Omega| - \int_{\Omega(t)} \boldsymbol{Q}\, d|\Omega|$$

The integral of fluxes over the domain boundary $\partial\Omega$ with the unit normal-vector $\boldsymbol{n}$ comprise the convective and viscous fluxes $\boldsymbol{f}$ and the flux due to grid-node velocities. The latter is approximated by a geometric conservation law [6]. The source term including $\boldsymbol{Q}$ results from the turbulent modelling.

The DLR TAU code employs an unstructured, edge-based cell-vertex finite volume discretization of equation (1) and equation (2) is evaluated by a node-centered numerical flux with the artificial-dissipation scheme by Jameson et. al [7]. The temporal discretization uses Jameson's dual time stepping of second-order accuracy [8]. The turbulence model can be chosen from a variety of one- and two-equation models.

In case of a forced-motion simulation, the time series of the coordinate vector $\boldsymbol{x}(t)$ corresponds to a deformation of the volume mesh. At each time step, the motion of the grid nodes on the surface boundaries results in a deformation which is propagated into the volume mesh by the help of radial basis functions [9][10]. The radial basis functions weigh the amount of deformation with the distance from the moving surface nodes. Thus, in the case of small deflections in comparison to the overall configuration, the method provides smooth deformations. The grid-node velocities at each time step correspond to the time-differentiated grid-node locations:

$$(3)\quad \boldsymbol{v}_g = \dot{\boldsymbol{x}}(t)$$

However, the grid-node velocities can represent additional flow velocities as it is considered in the field velocity approach proposed by [11]. This method is implemented in the DLR TAU code for gust analysis as the disturbance velocity approach (DVA) [12]. This approach is used to model gust encounters by directly inducing flow velocities in the flow field which correspond to a gust velocity-profile $\boldsymbol{w}(t)$. Thus, the grid-node velocities are the induced gust velocities but with inverse orientation:

$$(4)\quad \boldsymbol{v}_g = -\boldsymbol{w}(t)$$

By directly prescribing the grid-node velocities, the DVA cannot model the influence of the aircraft on the gust and hence it is a simplified model. Its accuracy, in comparison to a gust which is convected through the flow field, depends on the gust's wave length which should be at least greater than the reference chord length [13].

Consequently, the DVA yields to a similar treatment of gust encounters as of motion-induced flows by employing grid-node velocities $\boldsymbol{v}_g(t)$. However, for the gust analysis, the grid-node coordinates $\boldsymbol{x}$ remain time-invariant and the grid velocities are prescribed independently.

### 2.2. Linear System Identification

The method of linear system identification determines a system's dynamic response due to an arbitrary input signal by identifying the frequency response of the system. The linear frequency analysis allows finding the system's response by the multiplication of the frequency response function $G$ with the Fourier-transformed input signal $U$:

$$(5)\quad Y(i\omega) = G(i\omega)U(i\omega)$$

This is only valid for linear, time-invariant systems which impose the superposition principle for the input and output signals. This linearity in the dynamic response is virtually found for nonlinear systems, if the disturbances are sufficiently small. Thus, the time-linearized/small-disturbance approach allows identifying the dynamic flow field by the frequency response for small disturbances affecting the steady flow field [14].

Accordingly, the application of an impulse on the system and measuring its response results in the system's frequency response by rearranging equation (5):

$$(6)\quad G(i\omega) = \frac{Y_\delta(i\omega)}{U_\delta(i\omega)}$$

Considering a time-discretized system as described in section 2.1, the pulse input determines the quality of the obtained frequency response function. A short-time, small-amplitude pulse excitation is needed followed by long time series of zero excitation in order to compute the system's response. The length of the time signal $T$ defines the frequency resolution $\Delta\omega = \frac{2\pi}{T}$ of the frequency response function. The time-step size $\Delta t$ determines the maximum resolvable frequency, known as the Nyquist frequency, $\omega_N = \frac{2\pi}{2\Delta t}$. However, zero values in the frequency spectrum of the applied pulse signal further limit the frequency response's bandwidth, since it is the denominator of equation (6). Therefore, the pulse signal is defined by the

help of a smooth step function $s(t)$ compiling the ascent and the descent of the pulse:

$$(7)\quad \delta(t) = \begin{cases} s\left(\frac{t}{r\lambda}\right), & 0 \le t < r\lambda \\ s\left(\frac{-t+\lambda}{\lambda(1-r)}\right), & r\lambda \le t < \lambda \\ 0, & t \ge \lambda \end{cases}$$

The length of the non-zero part $\lambda$ is divided into the ascent and descent with $r$ specifying the ratio of the ascent's length. For $r = 0.5$ the shape of the pulse yields to zero values in the magnitude of the frequency spectrum. This is avoided for $r = 0.3$ which results in a smooth magnitude of the frequency spectrum, see Fig. 1. The smooth step function $s(t)$ is chosen to be a polynomial of fifth order.

The method's benefit is that the system to identify has not to be adapted for the time-linearized analysis. However, the validity of the dynamical linearity assumption has to be asserted by an amplitude study.

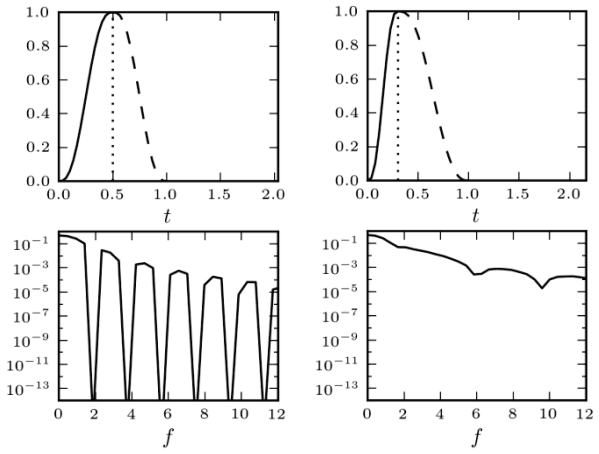


Fig. 1. Comparison of the pulse's shape and its corresponding magnitude of the frequency spectrum for $r = 0.5$ and $r = 0.3$ (vertical lines) displaying the ascent (solid) and descent (dashed) portion.

## 2.3. Linear Frequency Domain

The DLR TAU code possesses the linear frequency domain (LFD) solver which solves for the first-harmonic time-linearized/small-disturbance solution [3]. Instead of solving the fully nonlinear unsteady RANS equations, equation (1) is linearized around the steady mean state. The process of linearization includes the turbulence closure which is provided in the LFD solver for the one-equation turbulence model by Spalart and Almaras [15]. This is of importance, since a common simplification is to consider the eddy-viscosity to be time-invariant in the dynamically linear response [1]. The accuracy of this frozen eddy-viscosity approach has been demonstrated to decrease with increasing interaction between the shock and the boundary-layer [3] which renders its application unsuitable for transonic flows.

The derivation of the LFD equations evolves from the finite-volume discretized form of equation (1) as described in section 2.1:

$$(8)\quad \frac{d(\boldsymbol{MW})}{dt} + \boldsymbol{R}\left(\boldsymbol{W}, \boldsymbol{x}, \boldsymbol{v}_g\right) = 0$$

The integration matrix $\boldsymbol{M}$ consists of the discrete control volumes $|\Omega_i|$ which only depend on the grid-node coordinates.

Under the considered assumption of a predominately linear aerodynamic response due to a small-amplitude excitation, $\boldsymbol{W}$ can be separated into a time-invariant mean state $\overline{\boldsymbol{W}}$ and a time-dependent, small perturbation. Therefore, the linearization comprises a Taylor series expansion around the steady state which is truncated after the first-order term. Furthermore, by expressing the time-dependent perturbation in terms of a complex Fourier series expansion and moreover, only considering a first harmonic excitation and response, $\boldsymbol{W}$ can be approximated as:

$$(9)\quad \boldsymbol{W}(t) \approx \overline{\boldsymbol{W}} + \widehat{\boldsymbol{W}} e^{i\omega t}$$

Consequently, the time-dependent grid-node coordinates and velocities are approximated accordingly:

$$(10)\quad \boldsymbol{x}(t) \approx \overline{\boldsymbol{x}} + \widehat{\boldsymbol{x}} e^{i\omega t}$$

$$(11)\quad \boldsymbol{v}_g(t) \approx \widehat{\boldsymbol{v}_g} e^{i\omega t}$$

The time-invariant mean state $\overline{\boldsymbol{W}}$ is known by a steady-state RANS simulation employed on the reference grid $\overline{\boldsymbol{x}}$. The mean state of the grid-node velocities is considered to be zero, $\overline{\boldsymbol{v}_g} = 0$, for the investigated flows, although it is formally written for completeness.

By applying the truncated Taylor series expansion including equations (9) to (11) to the integration matrix $\boldsymbol{M}(\boldsymbol{x})$ and the residual $\boldsymbol{R}(\boldsymbol{W}, \boldsymbol{x}, \boldsymbol{v}_g)$, the terms of the linearized form of equation (8) are derived:

$$(12)\quad \boldsymbol{R}\left(\boldsymbol{W}, \boldsymbol{x}, \boldsymbol{v}_g\right) \approx \boldsymbol{R}\left(\overline{\boldsymbol{W}}, \overline{\boldsymbol{x}}, \overline{\boldsymbol{v}_g}\right) + \frac{\partial \boldsymbol{R}}{\partial \boldsymbol{W}}\Big|_{\overline{\boldsymbol{W}}, \overline{\boldsymbol{x}}, \overline{\boldsymbol{v}_g}} \widehat{\boldsymbol{W}} e^{i\omega t} + \frac{\partial \boldsymbol{R}}{\partial \boldsymbol{x}}\Big|_{\overline{\boldsymbol{W}}, \overline{\boldsymbol{x}}, \overline{\boldsymbol{v}_g}} \widehat{\boldsymbol{x}} e^{i\omega t} + \frac{\partial \boldsymbol{R}}{\partial \boldsymbol{v}_g}\Big|_{\overline{\boldsymbol{W}}, \overline{\boldsymbol{x}}, \overline{\boldsymbol{v}_g}} \widehat{\boldsymbol{v}_g} e^{i\omega t}$$

$$(13)\quad \boldsymbol{M}(\boldsymbol{x}) \approx \overline{\boldsymbol{M}}(\overline{\boldsymbol{x}}) + \frac{\partial \boldsymbol{M}}{\partial \boldsymbol{x}}\Big|_{\overline{\boldsymbol{x}}} \widehat{\boldsymbol{x}} e^{i\omega t}$$

The first term of equation (12) is the residual obtained by the steady-state RANS solution and thus, it is legitimate to presume:

$$(14)\quad \boldsymbol{R}\left(\overline{\boldsymbol{W}}, \overline{\boldsymbol{x}}, \overline{\boldsymbol{v}_g}\right) = 0$$

Finally, the application of equations (12) and (13) in equation (8) with the neglect of higher-order perturbation terms $\widehat{\boldsymbol{W}}\widehat{\boldsymbol{x}}$ yields to a linear equation system for the amplitude of the conservative variables $\widehat{\boldsymbol{W}}$:

$$(15)\quad \boldsymbol{A}\widehat{\boldsymbol{W}} = \boldsymbol{b}$$

The system matrix $\boldsymbol{A}$ comprises the steady integration matrix and the Jacobi matrix of the residual $\boldsymbol{R}$ evaluated at the steady state. The Jacobi matrix has been derived analytically for the DLR TAU code in the context of the discrete adjoint method [16].

$$(16)\quad \boldsymbol{A} = i\omega\overline{\boldsymbol{M}} + \frac{\partial \boldsymbol{R}}{\partial \boldsymbol{W}}\Big|_{\overline{\boldsymbol{W}}, \overline{\boldsymbol{x}}, \overline{\boldsymbol{v}_g}}$$

On the right-hand side (RHS) of equation (15), the vector $\boldsymbol{b}$ comprises the derivatives with respect to the grid-node coordinates and velocities:

$$(17)\quad \boldsymbol{b} = -\left(\frac{\partial \boldsymbol{R}}{\partial \boldsymbol{x}}\Big|_{\overline{\boldsymbol{W}}, \overline{\boldsymbol{x}}, \overline{\boldsymbol{v}_g}} + i\omega\overline{\boldsymbol{W}}\frac{\partial \boldsymbol{M}}{\partial \boldsymbol{x}}\Big|_{\overline{\boldsymbol{x}}}\right)\widehat{\boldsymbol{x}} - \frac{\partial \boldsymbol{R}}{\partial \boldsymbol{v}_g}\Big|_{\overline{\boldsymbol{W}}, \overline{\boldsymbol{x}}, \overline{\boldsymbol{v}_g}} \widehat{\boldsymbol{v}_g}$$

The derivatives of equation (17) are evaluated by central differences. The step sizes of the finite differences are the

perturbation amplitudes $\widehat{\boldsymbol{x}}$ and $\widehat{\boldsymbol{v}_g}$ which have to take account of the numerical errors implied by this approximation of the derivatives. The evaluation of analytically or automatically [17] obtained derivatives could remove this obstacle. The central differences are computed by evaluating the residuals with $\overline{\boldsymbol{W}}$ on the deformed mesh and with induced velocities. For building the central differences, the residuals have to be computed for the positive and the negative perturbation amplitude.

The linear system is solved iteratively by employing the Krylov generalized minimum-residual (GMRES) [18] scheme with the incomplete lower-upper (ILU) preconditioning [19]. The stability and efficiency of this solution technique regarding the properties of the resulting linear equation system has been demonstrated thoroughly for two- and three-dimensional forced-motion simulations in [3].

The RHS vector of equation (15) depends on the applied excitation. For a forced-motion simulation, the grid-node velocities are the time-differentiated coordinates, see equation (3). Thus, the perturbation amplitude on the grid velocities yields to $\widehat{\boldsymbol{v}_g} = i\omega\widehat{\boldsymbol{x}}$ and the RHS vector can be written as:

$$(18)\ \boldsymbol{b} = -\left(\frac{\partial \boldsymbol{R}}{\partial \boldsymbol{x}}\Big|_{\overline{\boldsymbol{W}},\bar{\boldsymbol{x}},\overline{\boldsymbol{v}_g}} + i\omega\left(\frac{\partial \boldsymbol{R}}{\partial \boldsymbol{v}_g}\Big|_{\overline{\boldsymbol{W}},\bar{\boldsymbol{x}},\overline{\boldsymbol{v}_g}} + \overline{\boldsymbol{W}}\frac{\partial \boldsymbol{M}}{\partial \boldsymbol{x}}\Big|_{\bar{\boldsymbol{x}}}\right)\right)\widehat{\boldsymbol{x}}$$

In case of the DVA, the grid-node coordinates are time-invariant. Consequently, for the perturbation follows $\widehat{\boldsymbol{x}} = 0$ and the RHS vector reduces to:

$$(19)\ \boldsymbol{b} = -\frac{\partial \boldsymbol{R}}{\partial \boldsymbol{v}_g}\Big|_{\overline{\boldsymbol{W}},\bar{\boldsymbol{x}},\overline{\boldsymbol{v}_g}}\widehat{\boldsymbol{v}_g}$$

The perturbation amplitude on the grid velocities $\boldsymbol{v}_g$ for the case of sinusoidal gust analysis is derived in section 3.2.

## 3. VALIDATION RESULTS

The time-linearized methods are validated by comparing the dynamic derivatives with time-accurate simulations employing the unsteady RANS equations as described in section 2.1. The time-domain results are transformed into the frequency domain with reference to the excitation amplitude in order to compute the transfer function at the simulated frequency of the sinusoidal excitation.

The validation is performed for a transonic test-case of the NACA 64A010 airfoil [20] at $Ma_\infty = 0.8$ and $Re_\infty = 12.5 \cdot 10^6$ with a mean angle of incidence $\bar{\alpha} = 0$. The turbulence model of Spalart and Allmaras [15] is employed. Both methods are validated for forced pitching oscillations around the $y$ axis at the airfoil's quarter point ($x = 0$). Additionally, the LFD solver is employed for sinusoidal gust encounters and validated against the Fourier-transformed time-domain results.

The NACA 64A010 is a symmetrical airfoil with a relative thickness of $10\%$ at $40\%$ of the airfoil's chord length $c$. Fig. 2 displays the two-dimensional computational grid in the vicinity of the airfoil. The unstructured grid of triangles is combined with a structured grid of quadrilaterals resolving the boundary layer. The far-field boundaries are in a radius of 100 chord lengths from the airfoil's quarter point. The computational grid consists of around $21.4 \cdot 10^3$ grid nodes.

In Fig. 3 the pressure distribution of the steady mean solution is presented. For the considered flow conditions, the flow around the airfoil remains attached.

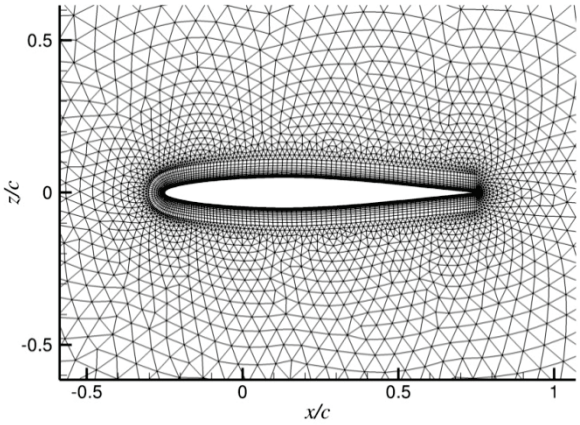


Fig. 2. Near-field grid around the NACA 64A010 airfoil with the chord length $c = 1.0$.

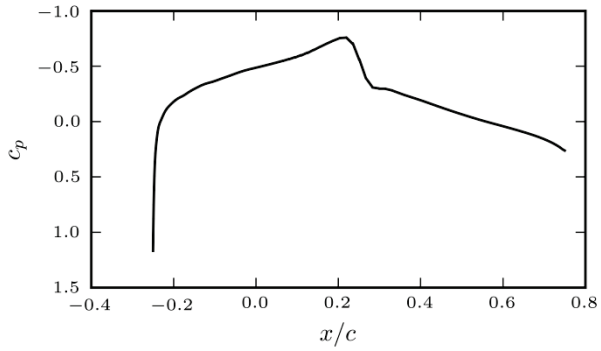


Fig. 3. Distribution of the steady pressure coefficient over the NACA 64A010 surface at $Ma_\infty = 0.8$, $Re_\infty = 12.5 \cdot 10^6$ and $\bar{\alpha} = 0$.

### 3.1. NACA 64A010 Pitching Oscillations

The forced pitching oscillations of the NACA 64A010 airfoil at the prior described flow conditions is a standard test case in the field of aeroelasticity [20]. The pitch oscillation is expressed in terms of the angle of incidence:

$$(20)\ \alpha = \hat{\alpha}\sin(\omega t)$$

The rotation is performed around the $\boldsymbol{y}$ axis at the airfoil's quarter point ($x = 0$). The angular frequency $\omega$ is expressed as the commonly presented reduced frequency which is defined non-dimensional by the chord length $c$ and the freestream velocity $U_\infty$:

$$(21)\ \omega^* = \omega\frac{c}{U_\infty}$$

For the validation of the presented time-linearized methods, the dynamic derivative of the lift coefficient $C_l$ is compared with the results of single-frequency sinusoidal time-domain simulations. The dynamic lift derivative is defined according to equation (6) by the help of Fourier analysis:

(22) $\hat{C}_{l_\alpha}(i\omega) = \frac{\mathrm{DFT}(C_l(t))}{\mathrm{DFT}(\alpha(t))}$

The discrete Fourier transformation (DFT) is computed by the Fast Fourier Transformation (FFT) algorithm [21]. The inverse transformation of the complex-valued derivative yields the time-dependent lift-coefficient in case of the sinusoidal oscillation of equation (20):

(23) $C_l(t) = \overline{C_l} + \mathrm{Re}(\hat{C}_{l_\alpha})\hat{\alpha}\sin(\omega t) + \mathrm{Im}(\hat{C}_{l_\alpha})\hat{\alpha}\cos(\omega t)$

In order to investigate the assumption of the dynamically linear response due to small perturbations, the time-accurate simulations are performed for a range of oscillation amplitudes. Fig. 4 shows the first harmonic of the dynamic lift coefficient for the reduced frequency $\omega^* = 0.2$. It exhibits a linear behavior up to the amplitude of approximately one degree. This long span of linear response region is found because of the moderate dynamic flow conditions at $\bar{\alpha} = 0$. For the following comparisons, the amplitude is chosen to $\hat{\alpha} = 10^{-3}$ degree.

Tab. 1 summarizes the employed simulation parameters for the harmonic time-domain simulations. A set of five pitching frequencies in the interval between 0.1 and 1.0 are computed. The time-step size is adapted to the frequency in order to ensure a consistent time-resolution of the harmonic response. Moreover, for each frequency five periods are computed for obtaining the flow-field's periodicity.

In contrast to the simulation of a fixed number of periods of the harmonic motion, it should be pointed out that convergence of the first harmonic may be reached earlier. Therefore, the Fourier analysis can be performed at each time step in order to monitor the convergence. For performing the Fourier analysis, a moving window approach must be applied which only accounts for the latter time steps assembling one period. Moreover, the application of a Cauchy criterion allows creating a termination criterion defined by a specified accuracy.

Tab. 1. Time-domain simulation parameters for the sinusoidal pitching oscillations.

| *Parameter* | *Value* |
|---|---|
| Number of time steps per period | 128 |
| Number of pseudo time iterations | 300 |
| CFL number (fine/coarse grid) | 40/10 |
| Multigrid cycle (level, type) | 4, w-sym |
| Number of periods | 5 |
| Reduced frequencies (5) | 0.1 – 1.0 |
| Amplitude $\hat{\alpha}$ | $10^{-3}$ deg |

Tab. 2. Time-domain simulation parameters for the pulse excitation

| *Parameter* | *Value* |
|---|---|
| Number of time steps per reference period[a] | 128 |
| Number of pseudotime iterations | 300 |
| CFL number (fine/coarse grid) | 40/10 |
| Multigrid cycle (level, type) | 4, w-sym |
| Number of time steps | 2500 |
| Amplitude $\hat{\alpha}$ | $10^{-3}$ deg |
| Pulse shape factor $r$ | 0.3 |
| Number of time steps of pulse | 128 |

[a]The reference period is chosen to be the highest considered reduced frequency $\omega^* = 1.0$.

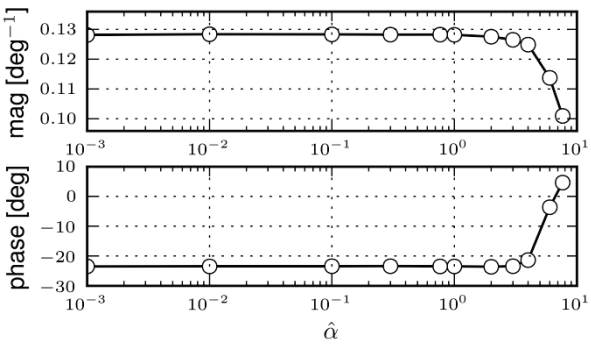


Fig. 4. Comparison of the dynamic lift derivative $C_{l_\alpha}$ from sinusoidal time-domain simulations for different pitch amplitudes in degree with a reduced frequency of 0.2.

### 3.1.1. Pulse excitation solutions

The identification of the dynamic response due to pitching oscillations for wide range of frequencies is obtained by the application of pulse signal of the airfoil's rotational motion. Thus, the excitation is the pulse signal as defined in equation (7) acting on the angle of incidence. From this time-domain simulation, the dynamic derivatives are found as for the sinusoidal time-domain simulations by equation (22). However, the flow response by employing time-accurate simulations may contain disturbances caused by numerical excitation. These can significantly flaw the response due to a pulse-like excitation because these can be of similar or greater magnitudes. Therefore, these disturbances are removed from the pulse's response by subtracting the non-excited time-dependent flow response. This process improves the accuracy of the numerical Fourier analysis.

In Tab. 2, the simulation parameters are summarized. These differ from the single-frequency simulations' parameters in the way the time-step size is chosen. The step size is defined by the number of time steps for the period of a reference frequency which is the highest frequency of interest. Furthermore, the simulated time length defined by the number of time steps has to resolve the aerodynamic response. Hence, the total number of time steps is much larger than those of the actual excitation.

The frequency response function obtained by the pulse excitation is presented in Fig. 5 for reduced frequencies in the interval from 0 to 1.2. Although the FRF is computed for much higher frequencies, up to the Nyquist frequency, see section 2.2. The time-step size may not appropriate to resolve these high frequencies. For the validation of the obtained FRF, the first harmonic of the dynamic lift derivative resulting from the time-accurate harmonic pitch simulation at five frequencies are shown. According to Fig. 5, excellent agreement between the obtained FRF and the time-domain solutions is achieved evincing the validity of the system identification approach.

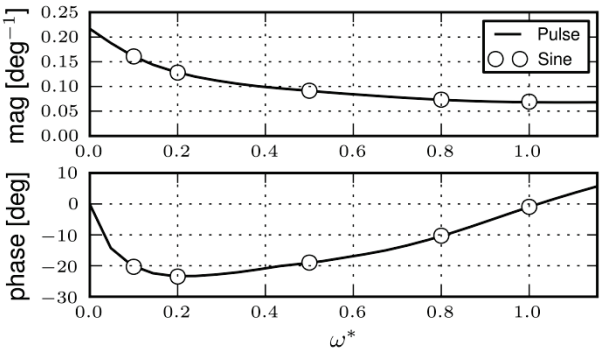


Fig. 5. Comparison of the frequency response of the dynamic lift derivative $C_{l_\alpha}$ obtained by the pulse excitation with the sinusoidal time-domain results.

The FRF is identified by assuming a dynamically linear behavior of the investigated flow due to a broadband signal of small amplitude. The requirements on the excitation signal have to be verified in the case that the time-accurate harmonic simulations are not known. This is achieved by convergence analyses of the simulation parameters. Alternatively, the requirements can be asserted by auxiliary time-accurate harmonic simulations.

For instance, the chosen pulse's amplitude is found to be on the lower end of the linear region of the harmonic simulation for the reduced frequency $\omega^* = 0.2$ and thus, it renders to be a feasible choice. In Fig. 6, the FRF is shown for different time-lengths of the pulse excitation specified by numbers of time steps. It displays no dependency of the FRF on the pulse's time length. In contrast, the length of the simulated time series is crucial for the accuracy of the FRF, since it determines the integrity of the response as well as the frequency resolution, see section 2.2. The convergence of the FRF is analyzed by the difference of its phase $\Delta\phi$ between two adjacent time samples $T_j$ and $T_{j-1}$ at selected frequency samples $\omega_n$:

$$(24)\ \Delta\phi\big(T_j, \omega_n\big) = \phi\big(T_j, \omega_n\big) - \phi(T_{j-1}, \omega_n)$$

The phase of the FRF measures the convergence best, since it exhibits the slowest rate of convergence in terms of degrees. In order to obtain the value of the FRF at the frequency sample, the FRF is interpolated with piecewise monotonic cubic polynomials [22]. Fig. 7 shows the convergence of the dynamic lift derivative's phase for the performed pitching oscillations. It displays a reduction of the relative phase error for the first time steps which is followed by a significantly slowed convergence. Although, the phase error decreases with increasing simulation time, it also displays a gradually slowing of the convergence behavior. Moreover, Fig. 7 shows higher errors for higher frequencies.

A comparison of the computational time between the method of system identification and the time-accurate harmonic simulation depends on the number and range of interested frequencies. In the considered case, five time-domain solution of 640 physical time steps are compared with one time-domain solution of 2500 physical time steps. However, the latter number has to be doubled if the undisturbed flow response is taken into account. Nevertheless, the accuracy of the FRF measured by the frequency resolution is much higher for the method of pulse excitation. For the considered frequency range, a reduction of computational time by more than a factor of 2.5 is achieved.

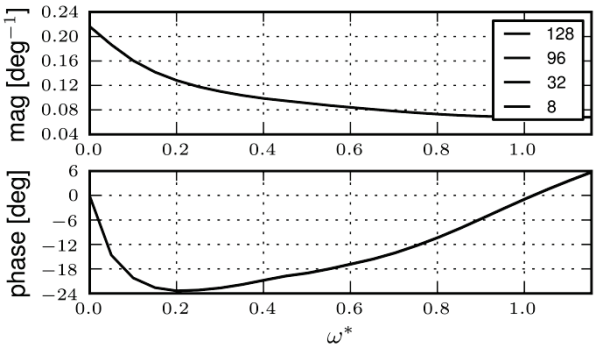


Fig. 6. Frequency response functions of the dynamic lift derivative $C_{l_\alpha}$ for different numbers of time steps composing the pulse's non-zero part $\lambda$ displaying the invariance due to the pulse's length.

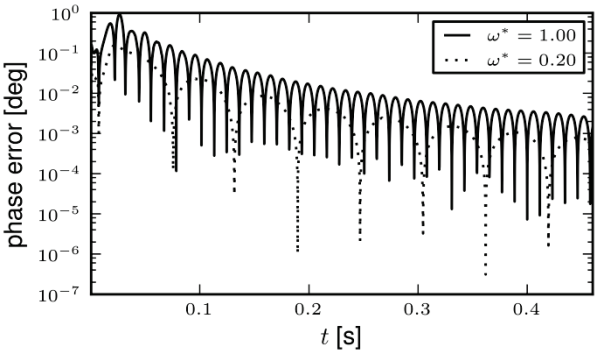


Fig. 7. Convergence of FRF's phase of the dynamic derivative $C_{l_\alpha}$ with increasing simulation time.

### 3.1.2. LFD solutions

The LFD method directly solves for the first-harmonic of the flow response due to a small-amplitude harmonic perturbation. The resulting linear equation system is solved iteratively as described in section 2.3. The system matrix is provided analytically and the RHS vector is defined by the amplitudes $\hat{\boldsymbol{x}}$ and $\widehat{\boldsymbol{v}_g} = i\omega\hat{\boldsymbol{x}}$. The harmonic perturbation $\hat{\boldsymbol{x}}$ is obtained by a grid deformation due to the airfoil's rotation around the $y$ axis with $\hat{\alpha}$. The derivatives of the residual are approximated by central differences and thus, the accuracy of RHS is dependent on the perturbation amplitude.

Tab. 3 lists the parameter for the LFD solutions. The amplitude of the pitch oscillation is found by an amplitude study, see Fig. 9. The dynamic lift derivative for the reduced frequency $\omega^* = 0.2$ is shown exhibiting constant results for amplitudes less than approximately $10^{-4}$ degrees. The derivation from the amplitude-independent behavior results from numerical errors due to the approximation of the RHS. Hence, for the lower amplitudes the linear equation system is solved for an approximately constant RHS vector. However, the numerical errors are small even for high amplitudes.

In Fig. 8, the frequency response function $\hat{C}_{l_\alpha}$ is shown at twelve frequencies and compared to the time-accurate harmonic results showing an excellent agreement. The employed preconditioned GMRES scheme for solving the linear equation system provides a high convergence rate. This results in reduction factor for the computational time of more than one magnitude in comparison to the time-accurate simulation of five periods of a sinusoidal pitch oscillation. However, the requirements on the computational memory significantly increase for solving the linear equation system. A detailed study of the computational time and memory requirements is performed in [3].

Tab. 3. LFD simulation parameters.

| *Parameter* | *Value* |
|---|---|
| Krylov GMRES iterations | 120 |
| Multigrid cycle (level, type) | single grid |
| Minimum residual abort criterion | $10^{-7}$ |
| Reduced frequencies (12) | 0.01 – 1.0 |
| Amplitude $\hat{\alpha}$ | $10^{-5}$ deg |

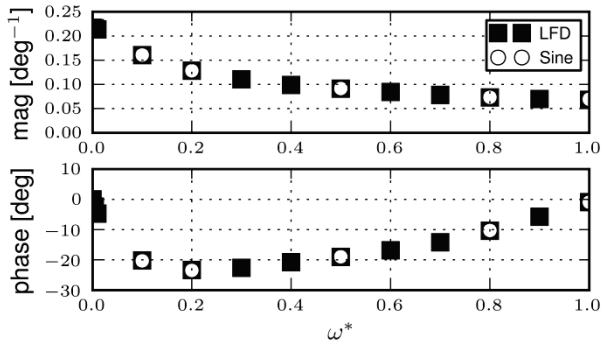


Fig. 8. Comparison of the frequency response of the dynamic lift derivative $C_{l_\alpha}$ obtained by the LFD with the sinusoidal time-domain results.

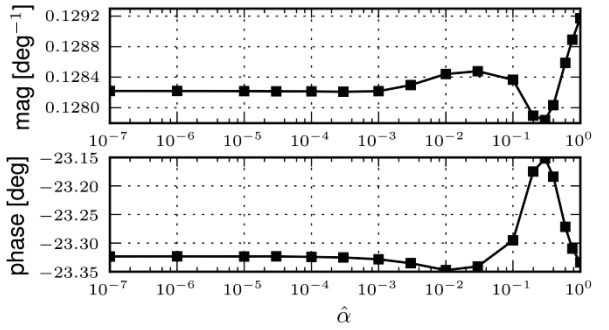


Fig. 9. Dynamic lift derivative $C_{l_\alpha}$ obtained by the LFD for the variation of the pitch amplitude at the reduced frequency $\omega^* = 0.2$ displaying the increasing numerical error due to the approximation of the RHS.

## 3.2. NACA 64A010 Sinusoidal Gust Encounter

The evaluation of sinusoidal gust encounters of small amplitude allows computing the dynamic derivatives with respect to the gust frequency. Fig. 10 depicts a sketch of the sinusoidal gust field around the airfoil. The gust field travels with the speed $U$ in the $x_i$ direction. Each point in the flow field experiences a sinusoidal change in the gust velocity $\boldsymbol{w}(x_i, t)$ with a constant frequency $\omega$ and a phase shift $\phi(x_i)$. The gust frequency is defined by the ratio of the gust translation-speed $U$ and the spatial wave length $\lambda$:

$$(25)\ \omega = \frac{2\pi U}{\lambda}$$

The phase shift is defined by a reference location $x_{i,0}$ and depends on the field point's coordinate $x_i$:

$$(26)\ \phi(x_i) = 2\pi \frac{x_{i,0} - x_i}{\lambda}$$

Taken together, the following equation for the gust velocity expresses a sinusoidal gust field in the time domain:

$$(27)\ \boldsymbol{w}(x_i, t) = \hat{\boldsymbol{w}} \sin\left(2\pi \frac{Ut + x_{i,0} - x_i}{\lambda}\right)$$

Equation (27) is transformed into the frequency domain yielding the complex-valued amplitude of the grid-node velocities for the sinusoidal gust field according to equation (4):

$$(28)\ \widehat{\boldsymbol{v}_g} = -\hat{\boldsymbol{w}} e^{i\phi(x_i)}$$

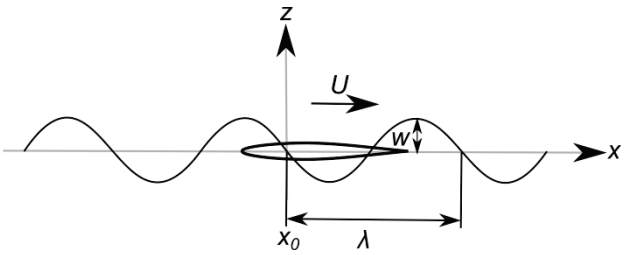


Fig. 10. Sketch of a vertical sinusoidal gust field.

The sinusoidal gust encounter for performing the validation is defined as a vertical gust field travelling over the NACA 64A010 airfoil as shown in the sketch of Fig. 10. The gust velocity $\boldsymbol{w}$ is directed in the $z$ direction and the gust field travels with the speed $U_\infty$ in the $x$ direction. Thus, the gust amplitude $\hat{\boldsymbol{w}}$ only comprises the $z$ direction. The phase shift $\phi$ of the field points depends on the $x$ coordinate and is defined with respect to $x_0 = 0$.

The simulation parameters for the time-accurate computations of the sinusoidal gust encounter and the pulse excitation are listed in Tab. 4. The aerodynamic pulse response is simulated for 2500 time steps. The LFD is employed with the parameters listed in Tab. 3. The RHS is computed with $\hat{\boldsymbol{x}} = 0$ and $\widehat{\boldsymbol{v}_g}$ as defined in equation (28). The gust amplitude is chosen to $\hat{w}_z = 10^{-5}\,\frac{\mathrm{m}}{\mathrm{s}}$.

In order to validate the results, the dynamic lift derivative $C_{l_\alpha}$ is computed according to equations (22) and (23). Therefore, the gust velocity is expressed in terms of a corresponding angle of incidence which results from the superposition with the constant gust translation-speed:

$$(29)\ \alpha = \arctan\left(\frac{w_z}{U_\infty}\right)\frac{180}{\pi}\,\mathrm{deg}$$

In Fig. 11 the frequency response function of the dynamic lift derivative is shown. The results obtained by both methods match with the dynamically nonlinear derivatives. However, small derivations for the LFD results are observed. Consequently, the pulse excitation method as well as the derived LFD approach is suited for computing the time-linearized flow response due to sinusoidal gust encounters.

Tab. 4. Simulation parameters for the time-accurate sinusoidal gust encounter and for the pulse excitation.

| *Parameter* | *Value* |
|---|---|
| Number of time steps per reference period[a] | 128 |
| Number of pseudo time iterations | 200 |
| CFL number (fine/coarse grid) | 40/10 |
| Multigrid cycle (level, type) | 4, w-sym |
| Amplitude $\widehat{w}_z$ | $10^{-5}$ m/s |

[a]The reference period is chosen to be the highest considered reduced frequency $\omega^* = 1.0$.

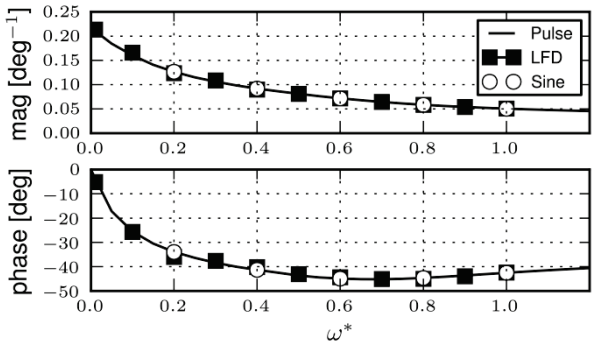


Fig. 11. The frequency response function of dynamic lift derivative $C_{l_\alpha}$ of the sinusoidal gust encounter obtained by the pulse excitation and the LFD compared with the dynamically nonlinear time-accurate solutions.

## 4. CONCLUSION

The simulation of forced motions and gust encounters with the DLR TAU code employing the unsteady RANS equations is presented in the context of harmonic analysis. Two methods for obtaining the time-linearized frequency response functions are described and validated by comparing the dynamic derivatives with the dynamically nonlinear time-accurate results of the DLR TAU code.

The validation is performed for harmonic pitch oscillations of the NACA 64A010 airfoil. The excellent agreement of the dynamic results is demonstrated in the limit of small amplitudes. Moreover, the reduction of computational time is discussed. However, the reduction strongly depends on the number and the range of the frequencies of interest. Although, the LFD solver exhibits the greatest reduction factors, since it directly solves for the harmonic small-perturbation response, the method of system identification may be better suited for broad frequency ranges. Moreover, the pulse excitation does not need the development of new solving routines employing directly the existing implementation of the nonlinear equations.

Furthermore, the sinusoidal gust encounter is derived for the LFD method and validated by comparison with the dynamically nonlinear time domain results. As well, the method of pulse excitation is employed for obtaining the FRF for gust encounters. Both methods show a very good agreement demonstrating the feasibility of the time-linearization approach for harmonic gust analysis.

The presented methods for simulating forced motion and gust encounters are bundled into one software package regarding the demonstrated underlying resemblance of the methodology. The software package is part of the FlowSimulator framework [23] which is a simulation environment for highly efficient and parallel multidisciplinary computations. The FlowSimulator framework provides an end-to-end interface to the DLR TAU code allowing full control over the simulation process.

## REFERENCES

[1] Chassaing, J.C., Gerolymos, G.A.: Time-Linearized Time-Harmonic 3-D Navier–Stokes Shock-Capturing Schemes. International Journal for Numerical Methods in Fluids, Vol. 56, No. 3, 2008, pp. 279–303

[2] Albano, E., Rodden, W.P.: A Doublet-Lattice Method for Calculating Lift Distributions on Oscillating Surfaces in Subsonic Flows. AIAA Journal, Vol. 7, No. 2, 1969, pp. 279–285

[3] Thormann R., Widhalm M.: Linear-Frequency-Domain Predictions of Dynamic-Response Data for Viscous Transonic Flows, AIAA Journal Vol. 51, No. 11, 2013

[4] Schwamborn, D., Gerhold, T., Heinrich, R.: The DLR TAU-Code: Recent Applications in Research and Industry. In proceedings of European Conference on Computational Fluid Dynamics, ECCOMAS CDF, Delft, The Netherland, 2006

[5] Hirt, C. W., Amsden A. A., Cook, J. L.: An Arbitrary Lagrangian-Eulerian Computing Method for All Flow Speeds. Journal of Computational Physics 14, 1974, pp. 227-53

[6] Mavriplis, D.J., Yang, Z.: Construction of the Discrete Geometric Conservation Law for High-Order Time-Accurate Simulations on Dynamic Meshes. Journal of Computational Physics, Vol. 213, No. 2, 2006, pp. 557–573

[7] Jameson, A., Schmidt, W., Turkel, E.: Numerical Solutions of the Euler Equations by Finite Volume Methods Using Runge–Kutta Time-Stepping Schemes. AIAA Paper 1981-1259, June, 1981.

[8] Jameson A: Time Dependent Calculations Using Multigrid, with Applications to Unsteady Flows Past Airfoils and Wings. In 10th Computational Fluid Dynamics Conference, Honululu, 24–26 June, 1991

[9] de Boer, A., van der Schoot, M.S., Bijl, H.: Mesh Deformation Based on Radial Basis Function Interpolation. Computers & Structures, Vol. 85, No. 2, 2007, pp. 784–795

[10] Barnewitz H., Stickan B.: Improved Mesh Deformation. In Management and Minimisation of Uncertainties and Errors in Numerical Aerodynamics: Notes on Numerical Fluid Mechanics and Multidisciplinary Design Volume 122, 219-243, 2013

[11] Singh, R., Baeder, J.D.: The Direct Calculation of Indicial Lift Response of a Wing Using Computational Fluid Dynamics. Journal of Aircraft, Vol. 35, No. 4, 1997, pp. 465–471

[12] Heinrich R., Michler A.: Unsteady Simulation of the Encounter of a Transport Aircraft with a Generic Gust by CFD Flight Mechanics Coupling. CEAS Conference, Menchester UK, 2009
[13] Heinrich R.: Simulation of Interaction of Aircraft and Gust Using the TAU-Code. In New Results in Numerical and Experimental Fluid Mechanics IX, Springer International Publishing, 2014, pp. 503-511
[14] Seidel D, Bennett R, Whitlow W Jr: An Exploratory Study of Finite Difference Grids for Transonic Unsteady Aerodynamics. 21st Aerospace Sciences Meeting, Reno, Nevada, 10–13 January, 1983
[15] Spalart P.R., Allmaras S.R.: A One-Equation Turbulence Model for Aerodynamic Flows. In 30th Aerospace Sciences Meeting and Exhibit, January 1992
[16] Dwight, R., Brezillon, J., Vollmer, D.B.: Efficient Algorithms for Solution of the Adjoint Compressible Navier–Stokes Equations with Applications. In Proceedings of the 7th ONERA-DLR Aerospace Symposium, edited by ODAS, Toulouse, France, 2006, pp. 1–11
[17] Griewank, A. Walther A.: Evaluating Derivatives: Principles and Techniques of Algorithmic Differentation. 2nd ed., Soc. For Industrial and Applied Mathematics, Philadelphia, 2008
[18] Saad, Y., Schultz, M.H.: GMRES: A Generalized Minimum Residual Algorithm for Solving Nonsymmetric Linear Systems. SIAM Journal on Scientific and Statistical Computing, Vol. 7, No. 3, 1986, pp. 856–859.
[19] McCracken, A.J., Timme, S., Badcock, K.J.: Accelerating Convergence of the CFD Linear Frequency Domain Method by a Preconditioned Linear Solver. In Proceedings of 6th European Congress on Computational Methods in Applied Sciences and Engineering, edited by Eberthardsteiner et. al., ECCOMAS 2012, Vienna, Austria, Sept. 2012
[20] Davis, S.: NACA 64A010 (NASA Ames model) oscillatory pitching. Compendium of Unsteady Aerodynamic Measurements AGARD R-702, 1982, pp. 2-1–2-22.
[21] Cooley, J.W., Tukey, J.W.: An algorithm for the machine calculation of complex Fourier series. Math. Comput. 19: 297-301, 1965
[22] Fritsch, F.N., Carlson, R.E.: Monotone Piecewise Cubic Interpolation. SIAM J. Numerical Analysis, Vol. 17, 1980, pp. 238-246
[23] Meinel, M., Einarsson, G.O.: The FlowSimulator framework for massively parallel CFD applications. In proceedings of PARA 2010, PARA2010, Reykjavik, Island, 6.-9. June, 2010.